Dynamic Nuclear Polarization Pulse Sequence Engineering using Single-Spin Vector Effective Hamiltonians

A. B. Nielsen,* J. P. A. Carvalho,* D. L. Goodwin, N. Wili, and N. C. Nielsen†
Interdisciplinary Nanoscience Center (iNANO) and Department of Chemistry, Aarhus University, Gustav Wieds Vej 14, DK-8000 Aarhus C, Denmark

Dynamic nuclear polarization (DNP) has proven to be a powerful technique to enhance nuclear spin polarization by transferring the much higher electron spin polarization to the nuclear spins prior to detection. While major attention has been devoted to high-field applications with continuous microwave irradiation, the introduction of fast arbitrary waveform generators is gradually increasing the opportunities to a realization of pulsed DNP. Here, we describe how static-powder DNP pulse sequences may systematically be designed using single-spin vector effective Hamiltonian theory. Particular attention is devoted to the intricate interplay between two important parts of the effective first-order Hamiltonian, namely, the linear field (single-spin) terms, and the Fourier coefficients determining scaling of the bilinear coupling terms mediating polarization transfer. We address two cases. The first operates in the regime where the microwave field amplitude is lower than the nuclear Larmor frequency. Here, we illustrate the predictive strength of single-spin vector model by comparing analytical calculations with experimental DNP results at 9.8 GHz/15 MHz on trityl radicals at 80 K. The second case operates in the high-power regime, where we combine the underlying single-spin vector design principles with numerical non-linear optimization to optimize the balance between the linear terms and the bilinear Fourier coefficients in a figure of merit function. We demonstrate, numerically and experimentally, a broadband DNP pulse sequence PLATO (PoLarizAtion Transfer via non-linear Optimization) with a bandwidth of 80 MHz and optimized for microwave field a with maximum (peak) amplitude of 32 MHz.

INTRODUCTION

Dynamic nuclear polarization (DNP) is transforming the field of nuclear magnetic resonance (NMR) by providing much higher sensitivity through transfer of polarization from the spins of free electrons to surrounding nuclear spins[1–7]. Moreover, by interfacing nuclear magnetic resonance (NMR) and electron paramagnetic resonance (EPR), DNP also offers the possibility to obtain information encoded by electron spins in addition to nuclear spin information. The electron spins typically involve much larger interaction strengths and, therefore, have sensitivity to the environment on longer distances. While most efforts at present are devoted to magic-angle-spinning (MAS) high-field DNP applications with the electron spins influenced by continuous-wave (CW) microwave (MW) irradiation, increasing attention emerges to the opportunities of realizing pulsed DNP. This is believed to significantly extend spin dynamics control, as seen earlier in the transformation of NMR from CW to pulsed operation.

Pulsed DNP comes with the need for design of optimal experiments which closely resemble the design of pulsed NMR experiments. However, there is a substantial difference concerning the much larger size of the electron-spin induced hyperfine coupling and the g-anisotropy interactions. This calls for design strategies which handle operations on the nanosecond timescale in addition to coping with interactions in the MHz to GHz regime. Furthermore, pulsed DNP requires instrumentation with very fast waveform generators and powerful MW amplifiers. This is at present found for instrumentation in the X-, Q-, and W-band MW regimes.[8–10] Using similar instrumentation, various pulsed DNP methods have already been demonstrated,[11] including NOVEL,[12] off-resonance NOVEL,[13] TOP,[14] XiX-DNP,[15] TPPM-DNP,[16] BEAM,[17] and frequency swept DNP.[18]

In this paper, we undertake the challenge of understanding the merits and design of pulsed DNP experiments within the regimes of pulsed low- and high-MW irradiation. Our approach will be based on our recent single-spin-vector effective Hamiltonian theory (SSV-EHT) method[19–21], which offers detailed insight into the spin dynamics and its associated control.

THEORY

In this section, we will introduce and discuss the relevant features of SSV-EHT needed to analyze and systematically develop advanced MW pulse sequences for static-powder DNP. This should be considered an easy-to-use and design-wise attractive alternative/supplement to average Hamiltonian theory,[22, 23] Floquet theory,[24, 25] and exact effective Hamiltonian theory,[26, 27] each of which have their strengths and weaknesses. Focusing on a basic understanding, rather than cumbersome algebraic derivations, the description is provided here in a picturesque fashion by using a bare minimum number of equations and instead concentrating attention to instruc-

* These authors contributed equally to this work.
† ncn@chem.au.dk

tive calculations and a pragmatic understanding. Additional insight and details of the mathematical concepts can be found in an earlier account on the theoretical basis of the SSV-EHT formalism.[19]

The Hamiltonian for a coupled electron (S) and nuclear (I) two-spin system can be expressed in the rotating frame of the electron and in the laboratory frame for the nuclear spin as

$$\hat{H}(t) = \Delta\omega_S \hat{S}_z + \omega_I \hat{I}_z + \hat{H}_{MW}(t) + A\hat{S}_z\hat{I}_z + B\hat{S}_z\hat{I}_x \ , \quad (1)$$

with $\Delta\omega_S$ denoting the electron spin offset, ω_I the nuclear Larmor frequency, and A and B the secular and pseudo-secular hyperfine coupling constants, respectively. We assume small g anisotropy and a point dipole model where $A = T(3\cos^2\theta_{PL} - 1)$ and $B = 3T\sin\theta_{PL}\cos\theta_{PL}$, with θ_{PL} being the angle between the principal axis system and the static magnetic field. T denotes the anisotropy of the hyperfine coupling. $\hat{H}_{MW}(t)$ describes a time-varying Hamiltonian for the applied MW pulse sequence. All frequencies are given as angular frequency units. With our focus being DNP of electron to nuclear polarization transfer. We do not apply any radio-frequency (RF) irradiation on the nuclear spins, as the size (and thereby the timescale) of the electron spin interactions largely overwhelm the corresponding interactions of the nuclear spins. We note that the first three terms in Eq. ((1) are single-spin, linear terms, and the final two terms, for the hyperfine coupling interaction, are bilinear spin terms.

When designing a pulse sequence which generates a time-independent effective Hamiltonian for the coupling terms in Eq. (1), driving coherence/polarization transfer between electron and nuclear spins, it is useful to describe the system in an interaction frame defined by the linear terms Eq. (1). These terms may be regarded as mediators of the transfer in addition to being the source of non-ideal pulse sequence behaviour, if not managed appropriately. Due to the commutation of nuclear and electron spin operators, i.e., $[\hat{I}_p, \hat{S}_q] = 0$ with p and q being x, y, or z, the frame transformation can be performed in any order. Since there is no RF irradiation on the nuclear spin, only the pseudo-secular $B\hat{S}_z\hat{I}_x$ hyperfine coupling term is being time-modulated with the nuclear Larmor frequency upon transformation. Therefore, generation of a finite first-order double-quantum (DQ) or zero-quantum (ZQ) effective Hamiltonian requires the time dependencies induced on the hyperfine coupling interaction, by the $\Delta\omega_S\hat{S}_z + \hat{H}_{MW}(t)\hat{S}_x$ terms, to counteract the modulation by the nuclear Larmor frequency. In this case time-independent terms exist for the hyperfine coupling in the interaction frame of the linear terms. Note that the DQ/ZQ operators for a given pulse sequence for easy interpretation may be defined in a tilted (or effective field) frame with the coherence/polarization transfer referred to as planar mixing. These are both commonplace in solid-state MAS NMR dipolar recoupling, establishing resonances between the MAS spinning frequency and the RF irradiation, and in pulsed DNP 'recoupling' experiments, establishing a resonance between the nuclear Larmor frequency and, e.g., the MW irradiation.

Importance of the linear field: Resonance and deviation

The simplest approach to generate a DQ or ZQ effective Hamiltonian is to use constant amplitude x-phase MW irradiation on the electron spins. Here, Figure 1 shows numerical simulations calculating the efficiency of electron to nuclear transfer, as function of the MW field strength, using $\hat{H}_{MW} = \omega_{MW}\hat{S}_x$ and an electron spin offset $\Delta\omega_S\hat{S}_z$. The mixing time has for each point been chosen as the shortest time providing maximal transfer. The simulations assumed a nuclear Larmor frequency of $\omega_I/(2\pi)$=15 MHz being in the regime of ^{1}H spins in a 0.35 T static magnetic field used for X-band EPR (9.8 GHz). In Fig. 1A, the transfer is mediated as $\hat{S}_x \rightarrow \hat{I}_z$ and in Fig. 1B as $\hat{S}_z \rightarrow \hat{I}_z$. From Fig. 1, it is clearly evident that for any polarization transfer to occur, the matching ('recoupling') condition with $\omega_I^2 = \Delta\omega_S^2 + \omega_{MW}^2$ needs to be fulfilled. Indeed, this is an efficient matching condition known as the NOVEL or off-resonance NOVEL condition[12, 13] with the transfer mediated as $\hat{S}_x \rightarrow \hat{I}_z$. For the far-offset case, the transfer is $\hat{S}_z \rightarrow \hat{I}_z$ which is commonly referred to as the Solid-Effect (SE).[28, 29] At the condition $\Delta\omega_S = \pm\omega_I$, no transfer of polarization to the nuclear spin occurs. This is the resonance condition for which $\omega_{MW} = 0$. In this case, the hyperfine interaction term in Eq. (1) will not be perturbed by the linear offset term of the electron spin. In general, a unit-less scaling factor $\kappa = \omega_{MW}/\sqrt{\Delta\omega_S^2 + \omega_{MW}^2}$ expresses the size of the bilinear DQ/ZQ effective Hamiltonian for constant amplitude MW irradiation. $\kappa = 1$ at the NOVEL condition and $\kappa = 0$ at the $\Delta\omega_S = \pm\omega_I$ condition.

It is important to realize that different conditions along the $\omega_I^2 = \Delta\omega_S^2 + \omega_{MW}^2$ matching condition for the CW irradiation scheme have different tolerances towards mismatching of the linear terms. The mismatches may occur due to wrong setting, inhomogeneity in the MW field over the sample volume or by g-anisotropies for the electron spins in a powder sample. Hence, it may be important to develop pulse schemes that are tolerant to variations in the resonance conditions. For the constant amplitude x-phase MW irradiation case, it can be seen to the left in Fig. 1 that the NOVEL condition ($\omega_{MW} = \pm\omega_I$, $\Delta\omega_S = 0$) is the most tolerant condition for efficient polarization transfer in terms of MW mismatch (horizontal changes) and electron spin offset frequency (vertical changes) by having a broader range around the matching condition for which transfer to the nuclear spin is still efficient. For the SE condition, using less MW power but requiring an electron offset, it can be seen in Fig. 1B that this condition is much narrower. The fact that the

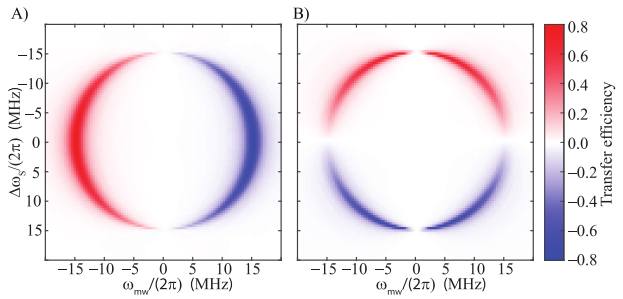

FIG. 1. Numerical simulation of the electron to nuclear spin polarization transfer as function of the field strength and electron spin offset in case of constant-amplitude, x- phase MW irradiation. The starting operator for the electron spin is along the $\hat{S}_x$-axis (A) or the $\hat{S}_z$-axis (B), while the detection operator for the nuclear spin in both cases is along $\hat{I}_z$. In the figures, the mixing time has been optimized for each offset/MW field for maximal absolute transfer. The calculations assumed an anisotropy of the hyperfine coupling of $T/(2\pi) = 1$ MHz and 20 uniformly distributed crystallite angles to mimic a powder sample.

NOVEL condition is less sensitive towards electron spin offset variations than the SE condition is not that surprising, as higher MW power is employed.

To further improve the stability towards mismatch in the resonance condition, one may take benefit from pulse sequences with varying phases and/or amplitudes. A simple, yet compelling example hereof demonstrating the potential of pulsed DNP is shown in Fig. 2A where three variants of the recent Broadband Enhanced Amplitude Modulation (BEAM) pulse sequence[17] are presented. For simplicity of the description, we have chosen settings that provide frequencies for which the matching conditions are easy to calculate, while noting that these settings do not lead to the best practically performing pulse sequences. The sequences span a time of $\tau_m = 50$ ns for their basic element, giving a modulation frequency of $\omega_m/(2\pi) = 1/\tau_m = 20$ MHz. The sequences are chosen to fulfil the resonance condition for a static field corresponding to a nuclear Larmor frequency of $\omega_I/(2\pi) = 15$ MHz. As the period τ_m of the basic element of the sequence, in this case, does not fulfil an integral number of rotations caused by the nuclear Larmor frequency, an effective nuclear linear field emerges. The size of this field may be described as

$$\omega^{(I)}_{lin,eff} = \omega_I - k_I\omega_m \quad \text{and} \quad k_I = \text{round}\left(\frac{\omega_I}{\omega_m}\right), \quad (2)$$

which for the pulse element in Fig. 2A amounts to $\omega^{(I)}_{lin,eff}/(2\pi)$= -5 MHz. Hence, addressing a 50 ns pulse element ($\omega_m/2\pi = 20$ MHz) that is repeated to provide the most efficient transfer for a given non-secular hyperfine coupling to a nuclear spin with Larmor frequency $\omega_I/(2\pi) = 15$ MHz, it is required that the effective linear field on the MW pulse element equals in size to $\omega^{(I)}_{lin,eff}/(2\pi)$. In this case, this corresponds to 5 MHz.

The effective linear field for a pulse sequence element may be expressed by the overall rotation angle θ_{tot} that the element will invoke on the electron spin operators scaled inversely by the period of the element, i.e., $\omega^{(S)}_{lin,eff} = \theta_{tot}/\tau_m$. The electron spin effective linear field may be defined as

$$e^{-i\omega^{(S)}_{lin,eff}\hat{S}^{eff}_z\tau_m} = \hat{\mathcal{T}}e^{-i\int_0^{\tau_m}\Delta\omega_S\hat{S}_z+\hat{H}_{MW}(t)dt}, \quad (3)$$

where $\hat{S}^{eff}_z$ denotes the tilted frame operator along which the effective field is oriented, $\omega^{(S)}_{lin,eff}$ its amplitude, and $\hat{\mathcal{T}}$ the Dyson time-ordering operator. In practice, the effective field in SU(2) may conveniently be be found using quaternions,[30] numerical calculations, or Exact Effective Hamiltonian Theory (EEHT)[26, 27] as described previously.[21] In the case of phase-inverted pulse sequences, as in Fig. 2A with red and blue squares representing x or $-x$ phase MW pulses, respectively, the linear field may easily be determined at zero offset for the electron spin ($\Delta\omega_S = 0$) as the pulse sequence commutes with itself at all times. Therefore, the total rotation angle caused by the element is just obtained by summing the rotation angle of each pulse in Fig. 2A with $\theta_{tot} = (\tau_x - \tau_{-x})\omega_{MW}$ in the ZQ case. For the three pulse sequences in Fig. 2, the MW field strengths are 25, 10, and 6.25 MHz and the phase changes happen after 20, 10, and 5 ns, respectively. The effective linear field is the same with $\omega^{(S)}_{lin,eff}/(2\pi) = (\tau_x - \tau_{-x})\omega_{MW}/(2\pi\tau_m) = 5$ MHz with $\tau_m = \tau_x + \tau_{-x}$.

By designing the pulse sequences to fulfil the condition $\omega^{(S)}_{lin,eff} = \pm\omega^{(I)}_{lin,eff}$, the linear fields for the two channels are matched, which gives the potential for good polarization transfer. This is indeed the case for the three pulse sequences in Fig. 2 where their respective transfer performances are numerically shown in Fig. 2B for a two-spin system with an anisotropy of the hyperfine coupling of $T/(2\pi) = 1$ MHz. The transfer efficiency depicted as function of mixing time is obtained by repeating the basic pulse elements using numerical calculations in black and by propagation using the first-order effective Hamiltonian found by SSV-EHT in red. It is seen that the fastest transfer occurs for the sequence on top, which also applies the highest MW amplitude. To understand the scaling factor for the DQ/ZQ effective Hamiltonian, it is useful to look at the Fourier coefficient presented in Fig. 2D), as described in the following section.

Importance of the bilinear field: Scaling and efficiency

Up to this point, the effect of the effective linear terms on DNP experiments taking electron spin coherence aligned along $\hat{S}_x$ (i.e., practically realized with a

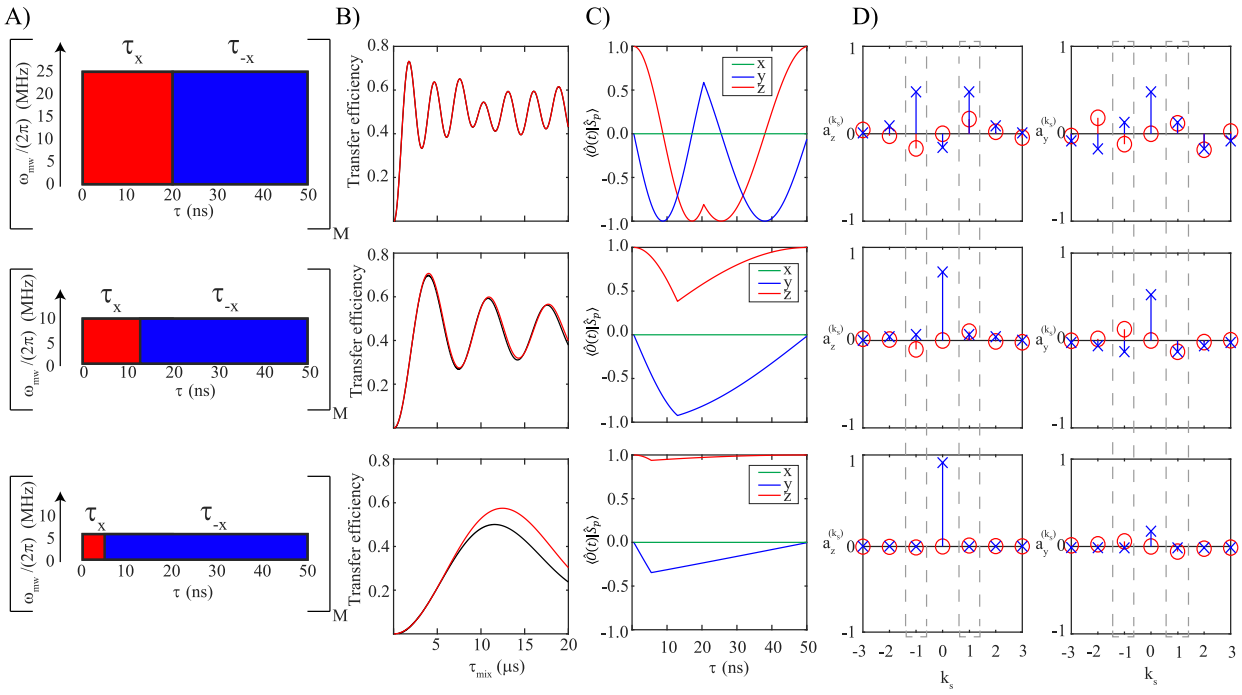

FIG. 2. A) Schematic representation of BEAM pulse sequences for static DNP under conditions of a nuclear Larmor frequency of 15 MHz. Red and blue colors represent x and $-x$ phase MW pulses of length τ_x and τ_{-x}, respectively. The overall length of the element is $\tau_m = \tau_x + \tau_{-x} = 50$ ns. The MW field strengths used are 25 MHz (top), 10 MHz (middle), and 6.25 MHz (bottom) with a total time for the basic pulse element of 50 ns. B) Numerical (black) and analytical (red) simulation of the transfer efficiency ($\hat{S}_x \rightarrow -\hat{I}_z$) for an electron-nuclear spin system as function of mixing time using the pulse sequences in A). The simulation is accomplished for a powder using 20 α,β crystallite angles and an anisotropy of the hyperfine coupling of $T/(2\pi) = 1$ MHz. C) Trajectories according to Eq. (4) for $\hat{S}_x$ (green), $\hat{S}_y$ (blue) and $\hat{S}_z$ (red) using the pulse sequences in A). D) Illustrates the Fourier coefficients $a_p^{(k_S)}$ for the three trajectories in C). The Fourier coefficients are calculated for the $p = z$ (left) and $p = y$ (right) with the real (blue cross) and imaginary part (red circles) mapped on a scale from -1 to 1.

$(\pi/2)_y$ preparation MW pulse) or along $\hat{S}_z$ (i.e., taken directly) into nuclear spin polarization (i.e., oriented along $\hat{I}_z$) has been investigated. This brought into attention that potential deviations from the resonance condition will effectively reduce the transfer efficiency for a given pulse sequence, how large the effect is, and simple means to remedy this. The other important parameter in experiment design is the scaling factor for the bilinear terms in the effective first-order Hamiltonian. This defines the time needed for (and thereby the time efficiency of) efficient polarization transfer. The shorter time, the less propensity of deleterious effects due to relaxation, multiple-spin effects, and mismatches in the effective linear fields.

In an SSV-EHT analysis, the scaling factor can be described in terms of trajectories for certain operators during the pulse sequence. In general, the trajectory for a certain operator influenced by a pulse sequence and potential offset will not be cyclic but lead to an overall rotation of the initial operator into another state by a rotation angle θ_{tot} as discussed above. However, the overall angle rotation can be disentangled by frame transformation and hereby cyclic trajectories appear with one characteristic frequency ω_m defined by the overall time of the trajectory. In the case where the hyperfine coupling interaction in Eq. (1) is the only bilinear term in the Hamiltonian, the only operator to track is the evolution of a starting operator $\hat{O}(0) = \hat{S}_z$ making up the electron spin operator of the hyperfine coupling interaction with operators $\hat{S}_z\hat{I}_z$ and $\hat{S}_z\hat{I}_x$. The evolution of the Hamiltonian components in the cyclic interaction frame can now be expressed as

$$\langle \hat{O}(t)|\hat{S}_p^{eff}\rangle = \sum_{k_S=-\infty}^{\infty} a_p^{(k_S)} e^{ik_S\omega_m t} \,, \qquad (4)$$

where p is either x, y, or z and $a_p^{(k_S)}$ the corresponding Fourier coefficients. In Figs. 2C and 2D, the trajectories in Eq. (4) and the corresponding Fourier coefficients are shown, respectively, with real (blue cross) and imaginary (red circles) coefficients for the three pulse sequences.

In the cyclic interaction frame of both the electron and nuclear spins, the Hamiltonian (cf., Eq. (1)) may be ex-

pressed as

$$\tilde{\hat{H}}(t) = \sum_{p=x,y,z} \sum_{k_S=-\infty}^{\infty} a_p^{(k_S)} e^{ik_S\omega_m t} \hat{S}_p^{eff} [A\hat{I}_z + \frac{B}{2}(e^{-ik_I\omega_m}\hat{I}^- + e^{ik_I\omega_m}\hat{I}^+)] - \omega_{lin,eff}^{(S)}\hat{S}_z^{eff} - \omega_{lin,eff}^{(I)}\hat{I}_z \ . \quad (5)$$

From Eq. (5), it is clear that only the matching values $k_S = \pm k_I$ contribute to the scaling factor for the DQ/ZQ effective first-order Hamiltonian. This is visualized in Fig. 2D by dashed boxes around the values $k_S = \pm 1$. It is clearly evident that by lowering the amplitude of the pulses, more of the $a_p^{(k_S)}$ coefficients are moved into the $k_S = 0$ band and hereby lowering the scaling factor. This is a straightforward consequence of $\sum_{k_S=-\infty}^{\infty} a_p^{(k_S)} = \langle \hat{O}(0)|\hat{S}_p\rangle$. A unitless scaling factor for DQ (+) or ZQ (-) bilinear terms can be defined as

$$a_{\mp} = \sqrt{(a_z^{(\mp k_I)} \pm a_y^{(\mp k_I)})(a_z^{(\pm k_I)} \mp a_y^{(\pm k_I)})} \ , \quad (6)$$

which for the pulse sequences in Fig. 2A give ZQ coefficients of $a_- = 0.60$ (top sequence), $a_- = 0.24$ (middle sequence), and $a_- = 0.06$ (bottom sequence), whereas the DQ coefficients are all zero. The scaling factors match well with the transfer efficiency plots in Fig. 2B, where the transfer is much slower for the low-power sequence. We note that the agreement between the full numerical calculated black curves and analytical red curves is getting worse for the sequence using less field strength. This is ascribed to higher-order terms, as we only have calculated first-order terms in the SSV-EHT calculation of the effective Hamiltonian.

Balancing linear and bilinear terms in numerical optimization

Up to this point, the effective Hamiltonian has been discussed as separated terms, namely the linear and the bilinear operator terms. To generate efficient pulse sequences coping with specific needs in regard of band-selective or broadbandedness relative to electron spin offsets, it is relevant to consider these terms in combination. This is ascribed to the fact that linear terms not commuting with the bilinear terms effectively truncates the effect of the latter ones as touched on earlier in relation to liquid- and solid-state NMR[19–21] and DNP.[17] Taking origin in the SSV-EHT approach[21] described above, we can readily define a figure-of-merit (FOM) function for transfer through the pseudo-secular hyperfine coupling as

$$\epsilon_{FOM} = \langle \rho(0)|\hat{S}_z^{eff}\rangle \frac{B^2 a_{\pm}^2}{B^2 a_{\pm}^2 + 4(\omega_{lin,eff}^{(S)} \pm \omega_{lin,eff}^{(I)})^2} \cdot \sin^2\left[\frac{\sqrt{B^2 a_{\pm}^2 + 4(\omega_{lin,eff}^{(S)} \pm \omega_{lin,eff}^{(I)})^2}}{4} t_{FOM}\right], \quad (7)$$

where + and − relates to transfers based on effective DQ and ZQ effective Hamiltonians, respectively, t_{FOM} the length of the overall pulse sequence, and the prefactor scaling through projection of the initial density operator onto the effective field axis.[17]

This formulation, which describes the evolution of the density operator in terms of the components of the effective Hamiltonian, has several crucial aspects relating to systematic pulse sequence engineering. First, through its direct relationship between the effective Hamiltonian, it is possible to optimize the capability of the bilinear terms in efficiently reaching polarization transfer with adherence to the time used for it. This is expressed through the $B^2 a_{\pm}^2$ coefficient which formulates the dependency of the pseudosecular hyperfine coupling strength (B) and the scaling through the Fourier coefficients ($a_{\pm}$) as described above. Second, it considers the truncating effects of the linear terms not commuting with the desired bilinear Hamiltonian as an inversion in either the ZQ or DQ invariant 3D subspace. The differential offset, which may be formulated as a fictitious $ZQ_z = I_z^{23} = (I_z - S_z)/2$ spin-1/2 operator,[31, 32] perturbs the ZQ transfer with a $(\omega_{lin,eff}^{(S)} - \omega_{lin,eff}^{(I)})$ dependency, while the sum of linear term frequencies $(\omega_{lin,eff}^{(S)} + \omega_{lin,eff}^{(I)})$ perturbs DQ inversion through the DQ fictitious spin-1/2 operator $DQ_z = I_z^{14} = (I_z + S_z)/2$ in the DQ subspace. This implies that the relevant linear terms need to be suppressed over the desired bandwidth of the pulse sequence. Third, the FOM equation above is extremely handy in optimizing pulse sequences as it may be work ahead in time, i.e., an effective Hamiltonian of a pulse sequence building block is predictive on the performance of a pulse sequence with repetition of the element a sufficient number of times M until it reaches the maximal transfer at $t_{FOM} = M\tau_M$.

The latter aspect proves extremely useful in non-linear optimization of pulse sequences as it may significantly reduce the number of free variables relative to previously demonstrated optimal control type optimizations[33–38] typically using hundreds to thousands of variables and presenting pulse sequences as lengthy arrays of amplitudes and phases. Such sequences may be difficult to interpret and may practically lead to concerns for the instrumentalists, as they do not leave much room for instrumental optimization and ready adaption to transfer via couplings with different size. While used mostly in relation to NMR and MRI experiment, op-

timal control theory has also been applied in the context of developing DNP experiments theoretically and numerically.[36, 39, 40] We will in the following demonstrate numerical and experimental results based on a simpler approach facilitated by the simplicity offered by the SSV-EHT FOM formulation appropriately balancing linear and bilinear terms in the effective Hamiltonian, and employing non-linear optimization. More specifically, a controlled random search [41–43] followed by optimization using the subplex routine [44] – a variant non-linear Nelder-Mead simplex optimization[45] with subspace search.

EXPERIMENTAL AND COMPUTATIONAL DETAILS

All experiments were conducted on a home-built X-band pulsed EPR/DNP spectrometer (based on the design of Doll *et al.* [8]) with a sample of 5 mM trityl (OX063) in a H_2O:D_2O:Glycerol-d_5 solution (1:3:6 by volume) at 80 K. Note that the degree of protonation in this system is higher than in the common DNP juice. A commercial MD4 electron-nuclear double resonance probe (Bruker BioSpin, Rheinstetten, DE) extended with an external tuning and matching circuit was used, and NMR signals were detected with a SpinCore iSpin-NMR console (SpinCore Technologies Inc., Gainesville, FL).

For all experimental data, the pulse sequence in Fig. 3A were used. For the initial saturation of ^{1}H, a set of $S = 11$ pulses of duration 2.4 μs separated by $\tau_{\mathrm{sat}} = 1$ ms were employed, while a solid-echo sequence $\pi/2 - \tau - \pi/2$ was used for read out with $\tau = 25$ μs (see Fig. 3A). All ^{1}H pulses used an RF field strength of 166.7 kHz and a $\pi/2$ pulse time of 1.5 μs. A 5 s overall pumping time with $P = 2500$ and $\tau_{rep} = 2$ ms were used for the experiments, if not specified otherwise. Experimental polarization enhancements reported in this work are denoted with ϵ_p which is defined by the ratio between the DNP-enhanced signal intensity and the thermal equilibrium signal intensity.

The optimization routine was developed using in-house written C++ scripts using the eigen3 template library.[46] The non-linear optimization routines were implemented using the NLOPT library.[47] The first optimization step consisted of a controlled random search [41–43] which was then refined using the subplex routine. [44] The sequence was optimized to cover a bandwidth of 80 MHz, in steps of 1 MHz, and considering a set of nine MW field strengths B_1/B_1^0 ={0.65, 0.70, 0.75, 0.80, 0.85, 0.90, 0.95, 1.00, 1.05} with corresponding weights ={0.079, 0.083, 0.088, 0.094, 0.103, 0.115, 0.135, 0.209, 0.095}, following a power-model to cope with MW field inhomogeneity. [48]

The numerical effective Hamiltonian considered in the optimization was calculated employing the matrix logarithm. The different components of Eq. (7) were calculated by computing the projections onto the desired operators, after the electron single-spin operators were rotated to ensure that the longitudinal electron single-spin operator is aligned with the effective field.

RESULTS AND DISCUSSION

In this section, we compare and discuss the analytical results relative to experimental findings. The section is split into two parts. The first operates in the regime where the MW field strength is lower than the nuclear Larmor frequency while the second addresses the high-power MW regime with design principles complemented with numerical non-linear optimization for development of offset compensated DNP pulse sequences.

Analysis of important parameters for efficient DNP transfer

The objective of this section is to illustrate the predictive power that a simple two-spin-oriented SSV-ETH analysis provides for developing efficient static DNP pulse sequences. We will compare analytical calculations of linear and bilinear operator terms to experimental DNP enhancement efficiencies, and discuss limitations in the model, in particular when a much larger spin system is required to understand the spin dynamics fully.

From Figure 2, we recall that the BEAM pulse element can be modified by lowering the required MW field strength while keeping the linear field constant to fulfil the resonance condition for efficient DNP transfer. To put further perspective to the predictive insight that an SSV-EHT-based model provides, we have in Fig. 3B investigated a permuted version of the BEAM element by analysing a two-BEAM-element pulse sequence, where the $-x$-phase irradiation is time shifted by Δt for the second element. By permuting the element, we ensure that the linear field will be independent of the time shifting Δt under conditions of on-resonance ($\Delta\omega_S = 0$) MW irradiation and thereby always fulfil the resonance condition. However, the size of the effective linear field, $\omega_{lin,eff}^{(S)}$ as a function of electron spin offset, $\Delta\omega_S$, will be different. In addition, the scaling factors of the bilinear fields, $a_{\mp}$, may change, as can be seen in Figs. 3C-E.

Figure 3C shows experimental ^{1}H DNP polarization enhancements ϵ_p, for three pulse sequences with $\Delta t =$ 0 ns (blue), $\Delta t = 25$ ns (red) and $\Delta t = 45$ ns (yellow) as function of mixing time, τ_{mix}. To compare the experimental results, we have in Figs. 3D-E calculated the transfer efficiency as function of τ_{mix} using the analytical calculated first-order effective Hamiltonian for a simple two-spin e-^{1}H spin system using a MW field strength of $\omega_{MW}/(2\pi) = 6.5$ MHz (D) and $\omega_{MW}/(2\pi) = 6.0$ MHz

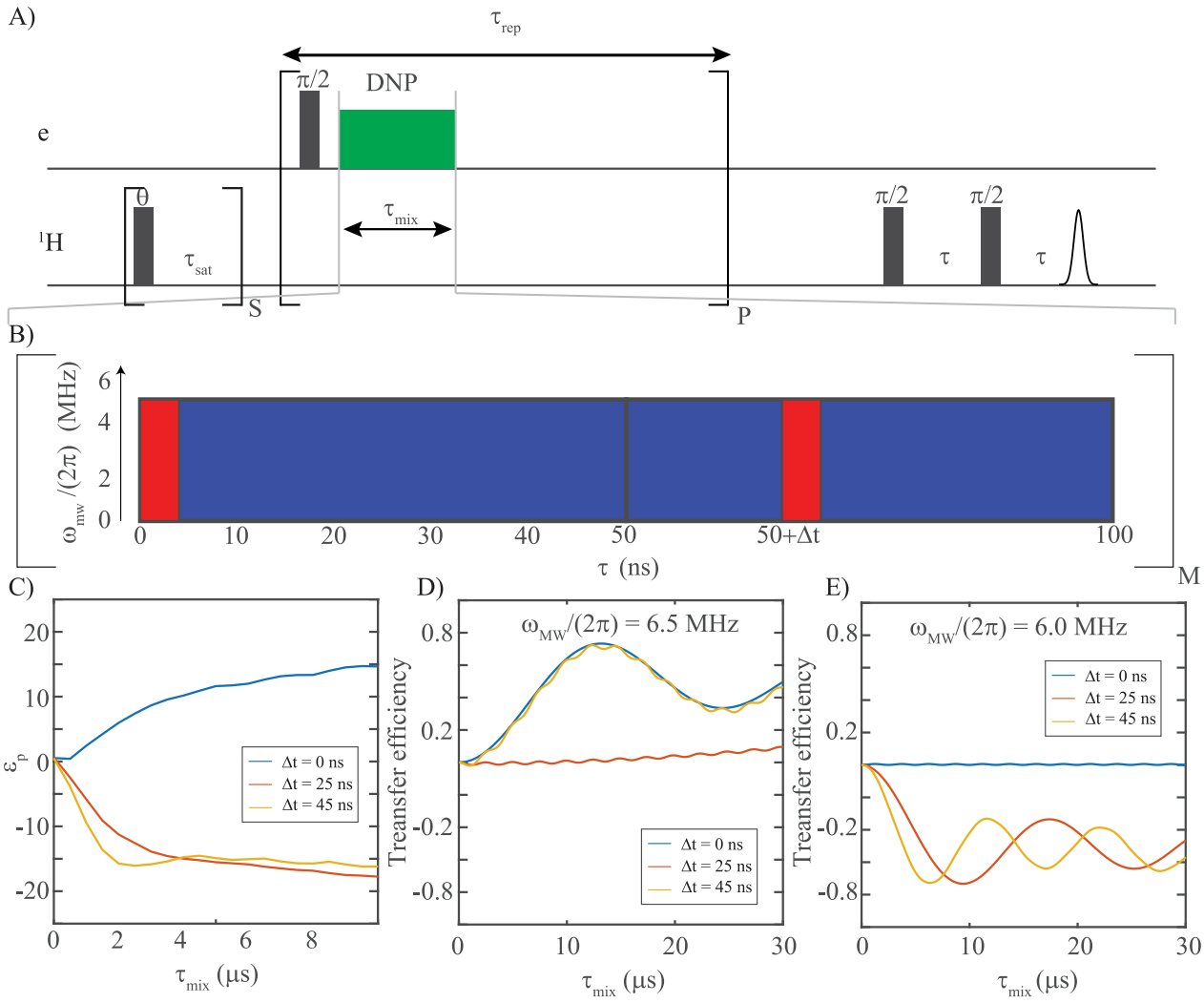

FIG. 3. A) Schematic representation of the pulse sequence used for e-^{1}H static DNP containing initial saturation pulses on the ^{1}H channel followed by a pumping element that is repeated P times for electron to nuclear polarization transfer and finally a solid-echo element for readout of the ^{1}H polarization. B) Illustration of the MW pulse element that is repeated M times to span the mixing period, $\tau_{mix} = M\tau_m$ with τ_m=100 ns. Colours red and blue indicate x and $-x$-phase MW irradiation, respectively. C) Experimental data for the ^{1}H signal enhancement, ϵ_p, as function of the mixing time τ_{mix} using the pulse element i B), Δt = 0 ns (blue), Δt = 25 ns (red) and Δt = 45 ns (yellow). An experimentally optimized MW field amplitude of 6.25 MHz was employed for Δt = 0 ns and 5.83 MHZ for Δt = 25 and Δt = 45 ns. The data were recorded using an overall pumping time of 5 s (τ_{rep} = 2 ms, P = 2500). D) and E) shows numerical simulations using the analytically calculated first-order effective Hamiltonian (evaluated at time points being an integral of $2\tau_m$) using an MW field strength of $\omega_{MW}/(2\pi)$ = 6.5 MHz in D) and $\omega_{MW}/(2\pi)$ = 6.0 MHz in E).

(E). The size of the anisotropy of the hyperfine coupling were set to $T/(2\pi)$ = 1 MHz.

From the experimental data in Fig. 3C, it can be seen that both positive (blue) and negative (red and yellow) polarization enhancements may be achieved depending on the time shifting. This can be explained by looking at propagation with the first-order effective Hamiltonian in Figs. 3D-E, analytically calculated for two elements, giving a total time of $2\pi/\omega_m$ = 200 ns. Relative to the idealized case addressed in section , the measurements were performed at a static magnetic field corresponding to a Larmor frequency of the ^{1}H nuclei of $\omega_I/(2\pi)$ = 14.8 MHz. By investigating the cyclic interaction frame Hamiltonian in Eq. (5) for a pulse sequence with $\omega_m/(2\pi)$ = 10.0 MHz, it becomes clear that resonance conditions exist at $\omega^{(I)}_{lin,eff}/(2\pi) = 4.8$ MHz and 5.2 MHz. This leads to either a ZQ condition at 5.2 MHz/0.8 = 6.5 MHz as shown in Fig. 3D or a DQ condition at 4.8 MHz/0.8 = 6.0 MHz shown in Fig. 3E. Indeed, this is in agreement with the experimental data using $\omega_{MW}/(2\pi)$ = 6.25 MHz and

where the $\Delta t = 0$ ns sequence (blue curves) produces a pure ZQ first-order effective Hamiltonian, the $\Delta t = 25$ ns sequence (red curves) almost a pure DQ first-order effective Hamiltonian, whereas the $\Delta t = 45$ ns sequence (yellow curves) contains both ZQ and DQ components but with different scaling factors as seen by the different buildup times for maximal transfers in Figs. 3D-E.

By comparing analytical and experimental curves, it is clear that several important features are well-described by the simple SSV-EHT-based two-spin model, which are useful for systematic design of efficient pulse sequences. The overall enhancement is better for the $\Delta t = 25$ ns sequence than for the $\Delta t = 0$ ns sequence. This can be explained by the larger scaling factor of the bilinear terms in the effective Hamiltonian. In addition, it can be seen that one should actively try to avoid having resonance conditions close to each other, fulfilling both ZQ and DQ conditions as is the case when $\Delta t = 45$ ns. This is especially important when dealing with large MW field inhomogeneities, where the specifics of such inhomogeneities are not sufficiently known to prevent overlap between the ZQ and DQ effective Hamiltonians for all inhomogeneity isochromats in the sample. In the current example, we still see a sizable amount of transfer, due to the magnitude of the DQ terms being approximately two times larger than the ZQ terms. However, as can be seen from the yellow curve in Fig. 3C, the polarization enhancement does not continuously increase as a function of the mixing time and, therefore, only a smaller overall enhancement is achieved compared to the red curve, despite having a larger scaling factor for the DQ terms.

Two aspects that the analytical model does not explain are: (*i*) the transient oscillations seen in the analytical curves are absent in the experimental data, and (*ii*) the experimental transfer efficiencies apparently exhibit a buildup rate that is approximately three times greater compared to the rates derived from the analytical curves. We attribute these two limitations primarily to the simplicity of the model, which approximates a large spin system to a two-spin model. In addition, defining the anisotropy of the hyperfine coupling to be $T/(2\pi) = 1$ MHz for the analytical calculations may also be inaccurate, relative to the real spin system. However, for the purposes of designing pulse elements for efficient DNP transfer, these two simplifications are not relevant for evaluating whether a given pulse sequence element is good or bad.

To further illuminate the design principles and how to systematically search for good pulse sequences, we have in Fig. 4 analysed another important parameter for the basic element, namely the overall time τ_m that the basic element takes. The basic element is shown in Fig. 4A using a constant MW field amplitude. For a pulse sequence to potentially provide good DNP polarization enhancement, it is required that the ratio between the lengths of -x-phase (red bar) and x-phase (blue) are chosen to match an effective linear field according to Eq. (5). This is ensured by setting the pulse durations τ_{-x} and τ_x to fulfill $\omega^{(S)}_{lin,eff} = (\tau_x - \tau_{-x})\omega_{MW}/\tau_m$ with $\tau_m = \tau_x + \tau_{-x}$.

Figure 4B displays the experimental polarization enhancement factors, while Figure 4C presents both numerical (solid lines) and analytical (dashed lines) polarization enhancement factors, ϵ_p, all as a function of the mixing time τ_{mix}. Three different modulation times, with $\omega_m/(2\pi) = 20$ MHz (black, $\tau_{-x} = 5$ ns, $\tau_x = 45$ ns), $\omega_m/(2\pi) = 18$ MHz (red, $\tau_{-x} = 14.5$ ns, $\tau_x = 41$ ns), and $\omega_m/(2\pi) = 16$ MHz (blue, $\tau_{-x} = 26.25$ ns, $\tau_x = 36.25$ ns) were examined. For the numerical and analytical calculations, the size of the anisotropy of the hyperfine coupling was again set to $T/(2\pi) = 1$ MHz. By comparing the numerical and experimental data, we observe a good correspondence between the initial buildup given by the scaling factor in Eq. (4). It can easily be seen that for $\omega_m/(2\pi) = 18$ MHz and 16 MHz, we obtain a higher scaling factor than for $\omega_m/(2\pi) = 20$ MHz. This correlates with a higher overall experimental polarization transfer of the ^{1}H spins, with maximal transfer efficiencies around $\epsilon_p = 23$ - 30, using a pumping time of 5 s. By using a longer pumping time of 60 s, we achieved an enhancement of approximately $\epsilon_p \sim 80$ (not shown). The size of DQ/ZQ scaling factor correlates with the ratio τ_x/τ_{-x} for the pulse element in Fig. 4A. Thus, when using a lower MW field strength than the ^{1}H Larmor frequency, the scaling factor in Eq. (4) will increase when the modulation time approaches the nuclear Larmor frequency. However, this also implies that the effective linear field on the electrons $\omega^{(S)}_{lin,eff}$ will be small to match the resonance conditions and thereby the ZQ and DQ conditions may both be active depending on the $a_\pm$ coefficients for a given pulse element.

A large linear field has the advantage that it truncates any unwanted ZQ or DQ bilinear terms. This effect is seen for the blue curves with $\omega_m/(2\pi) = 16$ MHz where the dotted blue curve in 4C is calculated using a first-order effective Hamiltonian for propagation. This effective first-order Hamiltonian does indeed contain both DQ and ZQ terms as the effective linear field is 1.2 MHz and not much larger than the size for the pseudo secular hyperfine interaction being 1 MHz. Therefore, the analytical first-order description does not converge that well and higher-order terms may be required for a precise description of the spin dynamics, as seen by comparing to the numerical calculated curve (solid blue line). From a pulse optimization point of view, this convergence is not problematic, as this situation will not lead to the best overall sequence. Experimentally, a better sequence was found for an element with a modulation frequency of $\omega_m/(2\pi)$ = 18 MHz and hereby requiring a larger effective linear field. This sequence is represented by the red curve in Figs. 4B and 4C.

As discussed in section , besides the scaling factors of

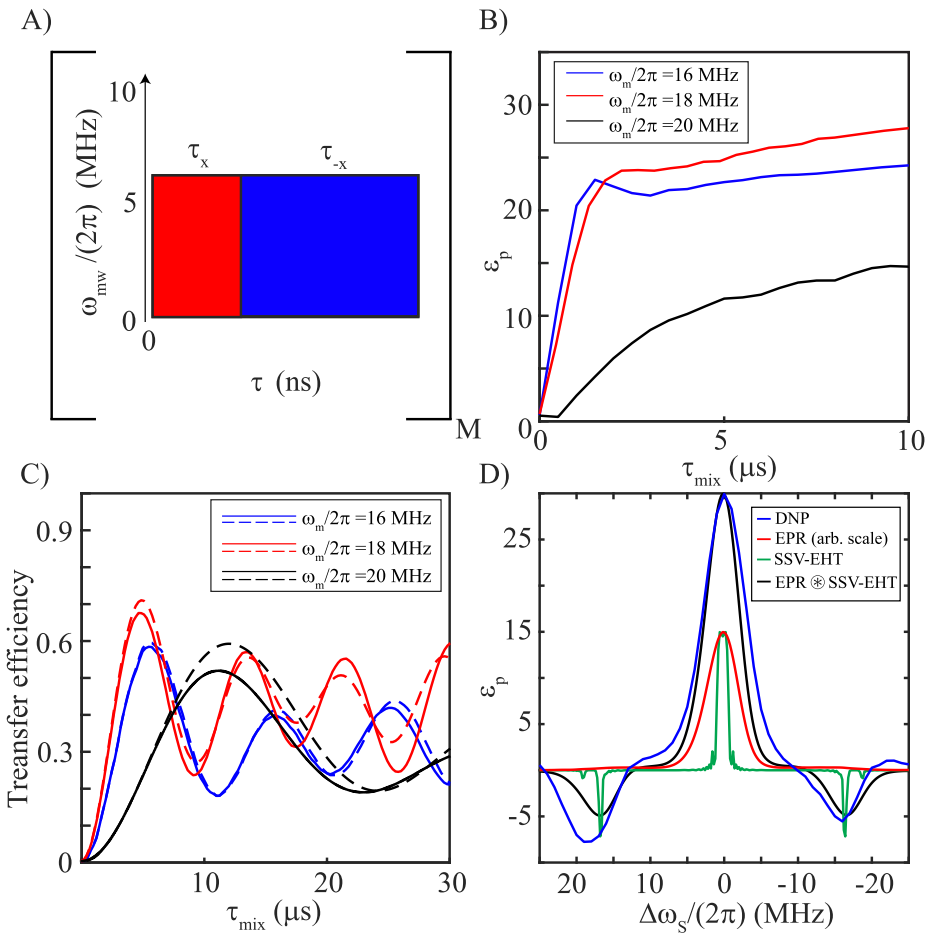

FIG. 4. A) Schematic representation of the pulse element used for e-^{1}H static DNP consisting of two pulses with -x phase (red) spanning a time period τ_x for the first pulse followed by a second pulse with x phase (blue) spanning a time period τ_{-x}. B) Experimental data for the DNP ^{1}H signal enhancement, ϵ_p, as function of mixing time τ_{mix} using the pulse element in A) with τ_{-x} = 5 ns, τ_x = 45 ns (black), τ_{-x} = 14.5 ns, τ_x = 41 ns (red) and τ_{-x} = 26.25 ns, τ_x = 36.25 ns (blue). Experimentally optimized MW field amplitudes of 6.25, 6.46 and 6.88 MHz were employed, respectively. C) Numerical (solid lines) and analytical (dashed lines) simulations of a two spin e-^{1}H system using the same pulse times as given in B) and a MW field strength of $\omega_{MW}/(2\pi)$ = 6.5 MHz (black), $\omega_{MW}/(2\pi)$ = 6.7 MHz (red) and $\omega_{MW}/(2\pi)$ = 7.5 MHz (blue). The analytical curves were calculated using the SSV-EHT first-order effective Hamiltonian. D) Experimental polarization enhancement (blue curve) as function of the electron offset $\Delta\omega_S/(2\pi)$ using the pulse times τ_{-x} = 14.5 ns, τ_x = 41 ns (red curves in B and C). The red curve shows the EPR line and the green curve shows the analytical calculated polarization transfer (both in arbitrary units). The black curve shows the folding of the red and green curve, with the maximum being normalized to match the blue curve.

the bilinear terms, it is also important that the effective linear field for a given pulse sequence does not vary much as a function of the electron spin offset, as this will influence the transfer efficiency. We have analysed this in Fig. 4D using the pulse sequence with $\omega_m/(2\pi)$ = 18 MHz (τ_{-x} = 14.5 ns, τ_x = 41 ns). In blue, is shown the experimental polarization enhancement ϵ_p, as function of electron spin offset. The green curve shows the analytical calculated transfer efficiency (arbitrary scaled for visualization) using a simple two-spin e-^{1}H spin system. It is clear that the resonance condition for the analytical calculated curves is much narrower than the experimental one.

However, by taking the line-width of the electron EPR signal, shown in red, into account, good agreement with the experimental data can be achieved. This demonstrated by the black curve (B) which has been calculated by folding the red (R) and green (G) lines using $B(\omega) = \int R(\omega)G(\omega - \Delta)d\Delta$. In this way, from a simple analytical model and the EPR spectrum, we show it is possible to predict the efficacy of a pulse sequence, particularly since unwanted offset effects may also be considered. More specifically, the negative transfers that occur at an electron spin offset of $\Delta\omega_S/(2\pi) = \pm 15$ MHz, may lead to destructive interference with the positive transfer at zero offset and, therefore, should be to be avoided.

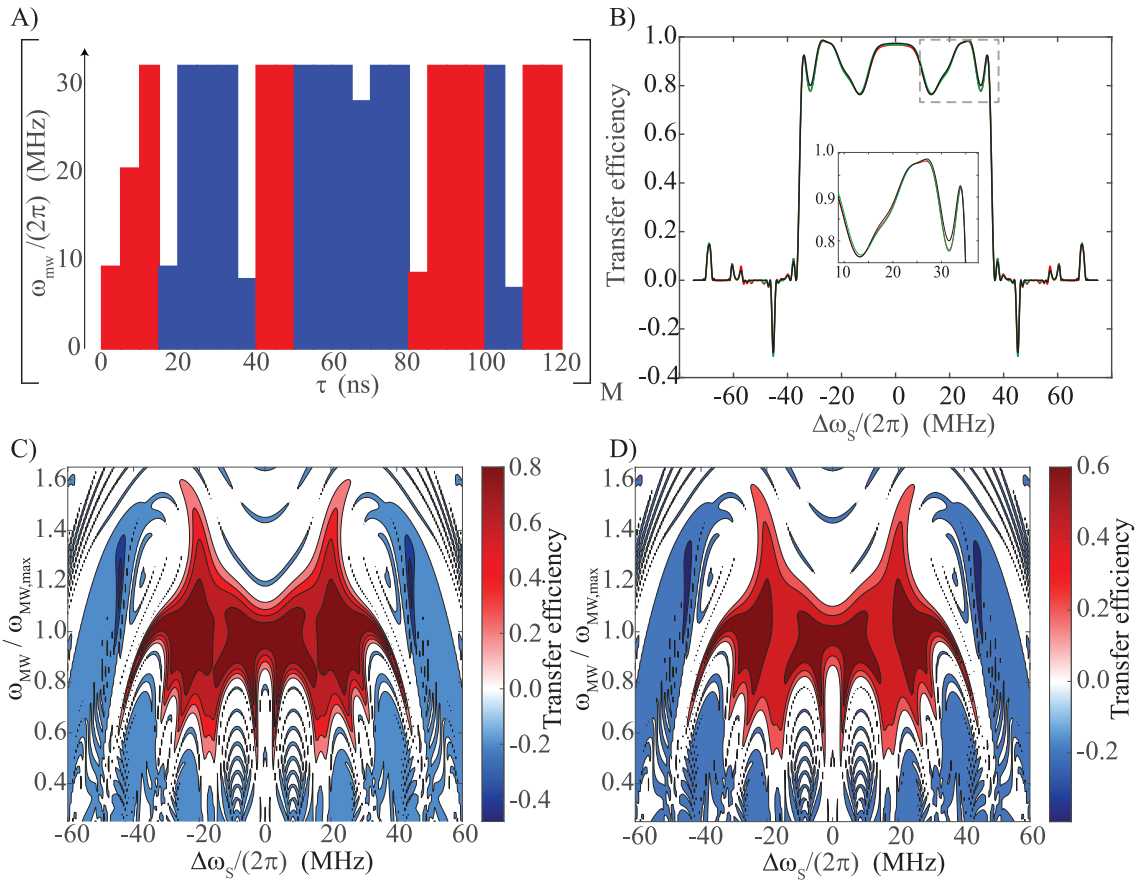

FIG. 5. A) Schematic representation of the PLATO pulse element developed using a non-linear optimization approach for e-^{1}H static DNP with the pulse amplitude (in MHz) for individually pulses. Red and blue illustrates x and $-x$ phase pulses, respectively (the amplitudes of the 24 5-ns pulses are {9.31, 20.36, 32.00, -9.29, -32.00, -32.00, -32.00, -7.86, 32.00, 32.00, -32.00, -32.00, -32.00, -28.04, -32.00, -32.00, 8.60, 32.00, 32.00, 32.00, -32.00, -6.94, 32.00, 32.00} MHz). B) Analytically derived FOM vs electron spin offset ($\Delta\omega_S/(2\pi)$) profile (Eq. (7)) overlaid with the corresponding profile calculated for the density operator. C) and D) 2D density operator transfer profiles as function of electron spin offset ($\Delta\omega_S/(2\pi)$) and the MW field amplitude ($\omega_{MW}/(2\pi)$). The calculations in B-D) assumed an e-^{1}H two-spin system with an anisotropy of the hyperfine coupling of $T/(2\pi)$ = 1 MHz (corresponding to an inter-spin distance of r_{eH}=4.5 Å in a point-dipole model), a static magnet field of B_0=0.35 T, and total mixing time of 2.28 μs (representing M=19 repetitions of the basic 120 ns element in A). In C) a single crystallite orientation was considered, such that $A/(2\pi) = -0.4$ and $B/(2\pi) = 1.0$ MHz, while a powder represented by 20 crystallite angles was considered in D).

For this analytical analysis, this only leads to a marginal loss in the highest polarization transfer, occurring at zero offset.

Offset compensation by non-linear optimization

In the previous section, we discussed the requirements for designing good pulse sequence elements balancing linear and bilinear terms in the SSV-EHT effective Hamiltonian. Taking a numerical approach to develop efficient broadband DNP experiments, we here demonstrate non-linear optimization of ϵ_{FOM} as formulated in Eq. (7) considering both ZQ and DQ formulations simultaneously. The objective has been to design an efficient e-^{1}H DNP pulse sequence with a bandwidth of 80 MHz (for the electron spin offset, $\Delta\omega_S/(2\pi)$) using a maximal (peak) MW amplitude of 32 MHz. We used a digitization of the pulses in 5 ns steps with 24 pulses over a DNP building block period of 120 ns corresponding to a modulation frequency of $\omega_m/(2\pi) = 8.33$ MHz. By inspecting Eq. (2), it is seen that this corresponds to a linear effective field of around $\omega^{(I)}_{lin,eff}/(2\pi) = 1.9$ MHz which will provide a good truncation of unwanted ZQ or DQ terms.

Combining non-linear optimization, numerical analysis, and experimental measurements, we obtained results as demonstrated in Fig. 5. The optimal pulse sequence - henceforth denoted PLATO (PoLarizAtion Transfer via non-linear Optimization) - was obtained by optimization of ϵ_{FOM} for a single crystal orientation with

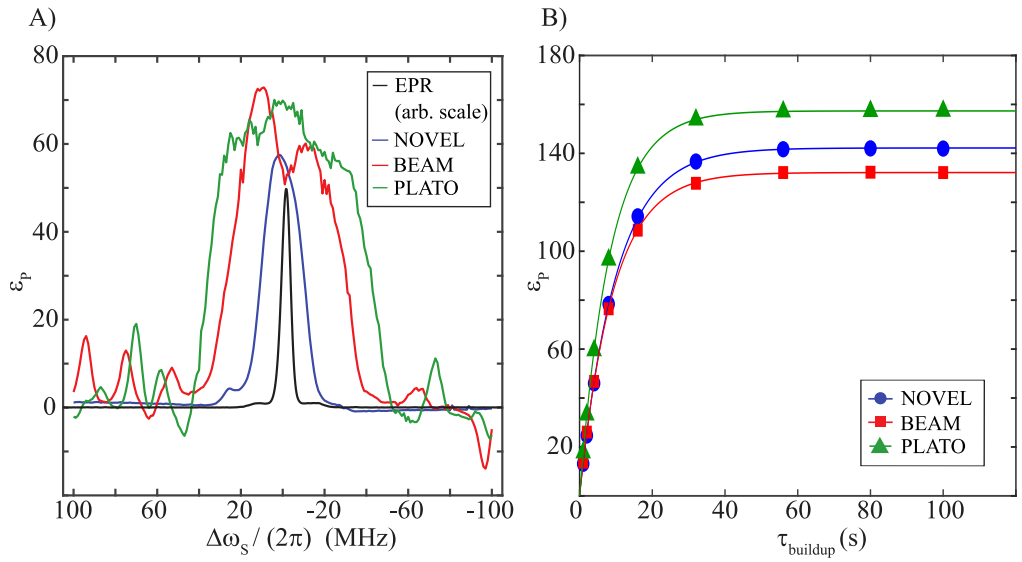

FIG. 6. A) Experimental data for the ^{1}H signal enhancement, ϵ_p, for NOVEL (blue), BEAM, with $\tau_x = 20$ and $\tau_{-x} = 28.75$ ns, (red) and PLATO (green) as function of electron spin offset, $\Delta\omega_S/(2\pi)$ using a buildup time of 5 s. The black curve shows the experimental EPR signal. B) Experimental ^{1}H enhancement factors as function of pumping time ($\tau_{\text{buildup}} = P\tau_{\text{rep}}$) using the same pulse sequences as in A). The buildup times T_B, given by $\epsilon_p(\tau_{\text{buildup}}) = \epsilon_{\max}[1 - \exp(-\tau_{\text{buildup}}/T_B)]$ for NOVEL, BEAM and PLATO correspond to 10.0, 9.2, and 8.4 s. All experimental data was acquired using experimentally optimized mixing times, τ_{mix}, of 2000, 585, and 720 ns for NOVEL, BEAM, and PLATO, respectively, and MW field amplitudes ($\omega_{MW}/(2\pi)$) of 16.25 MHZ for NOVEL and 36.25 MHZ for BEAM and PLATO.

$A/(2\pi) = -0.4$ MHz and $B/(2\pi) = 1.0$ MHz, initial S_x operator (prepared by the $(\pi/2)_y$ pulse), x-phase MW irradiation (allowing positive and negative amplitudes) and under consideration of an experimentally relevant MW field inhomogeneity profile (see section 3) is shown in Fig. 5A. The FOM function calculated using either SSV-EHT (black curve) or by projection of a numerical effective calculated Hamiltonian (red) and the state-to-state calculation (green) at $t_{FOM} = 2.3$ μs (expectation value $\langle I_z\rangle(t)$) is plotted as a function of the electron spin frequency offset $\Delta\omega_S/(2\pi)$ in Fig. 5B. The corresponding density operator projection is shown as a function of the electron spin offset and the MW amplitude ($\omega_{MW}/(2\pi)$, with the nominal maximum value being 32 MHz) for a single crystal and a powder in Figs. 5C and 5D, respectively. We note the extreme broadbandedness of the PLATO pulse sequence exceeds previously demonstrated DNP pulse sequences.

Figure 6 shows experimental results obtained for the PLATO DNP sequence optimized in Fig. 5 in comparison with results obtained for previously proposed NOVEL and BEAM pulse sequences and the profile of the EPR resonance. It is clearly evident that the PLATO pulse sequence developed by balancing linear and bilinear terms in the FOM function by non-linear optimization is more broadbanded than the compared methods, and that the developed pulse sequence works very well experimentally. The latter is extremely important, as it is well-known that the electron-nuclear spin systems in typical DNP cases, as here explored for trityl, are much larger than a two-spin model. We attribute this result to optimization of the effective Hamiltonian, rather than state-to-state optimization often used in typical numerical (e.g., optimal control) optimizations. We should note that our comparison dealt with sequences not further improved by adiabatic implementation, which may render all the individual compared methods more broadbanded.

CONCLUSIONS

In this work, we have theoretically, numerically, and experimentally demonstrated how the single-spin vector effective Hamiltonian (SSV-EHT) approach can be used to understand and design pulse sequences for static DNP by investigating single-spin operators in a two-spin system. By analysing the terms in the first-order effective Hamiltonian giving rise to the linear fields (single-spin terms) and the Fourier coefficients that describe the scaling factors for the bilinear terms (two-spin terms), we were able to establish the crucial parameters that provide insight in the experimental transfer performance for a given pulse sequence.

Based on the same principles, we designed an extremely broadbanded DNP pulse sequence, PLATO, employing a non-linear optimization. The PLATO DNP

sequence covers an electron spin offset range of approximately 80 MHz using a maximum MW field strength of 32 MHz. This may open up for the possibility to explore other radicals with a larger linewidth for efficient polarization transfer to nuclear spins in DNP experiments.

AUTHOR CONTRIBUTIONS

All authors designed the research. J.P.A.C. and A.B.N. performed all experiments supported by N.W. A.B.N., N.C.N., N.W., and J.P.A.C. developed the theory. N.W. built the spectrometer. A.B.N. and J.P.A.C wrote simulation scripts and did numerical calculations supported by N.C.N and D.L.G. All contributed to writing the manuscript.

CONFLICTS OF INTEREST

There are no conflicts to declare.

DATA AVAILABILITY

Data for this article, including experimental data and code for evalutation/optimzation of pulsed DNP experiments (compiled code and input files) are available at Zenodo at https://doi.org/10.5281/zenodo.13143783.

ACKNOWLEDGEMENTS

We acknowledge financial support from the Aarhus University Research Foundation (Grant AUFF-E-2021-9-22), the Swiss Natural Science Foundation (Postdoc.Mobility grant 206623), the Villum Foundation (Grant 50099), the Novo Nordisk Foundation (Grant NNF22OC0076002), and the DeiC National HPC (g.a. DeiC-AU-L5-0019).

[1] T. R. Carver and C. P. Slichter, Polarization of nuclear spins in metals, Phys. Rev. **92**, 212 (1953).
[2] A. W. Overhauser, Polarization of nuclei in metals, Phys. Rev. **92**, 411 (1953).
[3] A. Abragam, *The Principles of Nuclear Magnetism*, International series of monographs on physics (Clarendon Press, 1961).
[4] L. R. Becerra, G. J. Gerfen, R. J. Temkin, D. J. Singel, and R. G. Griffin, Dynamic nuclear polarization with a cyclotron resonance maser at 5 t, Phys. Rev. Lett. **71**, 3561 (1993).
[5] J. H. Ardenkjær-Larsen, B. Fridlund, A. Gram, G. Hansson, L. Hansson, M. H. Lerche, R. Servin, M. Thaning, and K. Golman, Increase in signal-to-noise ratio of > 10,000 times in liquid-state nmr, Proceedings of the National Academy of Sciences **100**, 10158 (2003).
[6] A. S. Lilly Thankamony, J. J. Wittmann, M. Kaushik, and B. Corzilius, Dynamic nuclear polarization for sensitivity enhancement in modern solid-state nmr, Progress in Nuclear Magnetic Resonance Spectroscopy **102-103**, 120 (2017).
[7] I. B. Moroz and M. Leskes, Dynamic nuclear polarization solid-state nmr spectroscopy for materials research, Annual Review of Materials Research **52**, 25 (2022).
[8] A. Doll and G. Jeschke, Wideband frequency-swept excitation in pulsed epr spectroscopy., J Magn Reson **280**, 46 (2017).
[9] T. Bahrenberg, Y. Rosenski, R. Carmieli, K. Zibzener, M. Qi, V. Frydman, A. Godt, D. Goldfarb, and A. Feintuch, Improved sensitivity for w-band gd(iii)-gd(iii) and nitroxide-nitroxide deer measurements with shaped pulses, Journal of Magnetic Resonance **283**, 1 (2017).
[10] M. V. H. Subramanya, J. Marbey, K. Kundu, J. E. McKay, and S. Hill, Broadband fourier-transform-detected epr at w-band, Applied Magnetic Resonance **54**, 165 (2023).
[11] K. O. Tan, S. Jawla, R. J. Temkin, and R. G. Griffin, Pulsed dynamic nuclear polarization (John Wiley & Sons, Ltd, 2019) pp. 339–352.
[12] A. Henstra, P. Dirksen, J. Schmidt, and W. Wenckebach, Nuclear spin orientation via electron spin locking (novel), Journal of Magnetic Resonance (1969) **77**, 389 (1988).
[13] S. K. Jain, G. Mathies, and R. G. Griffin, Off-resonance NOVEL, The Journal of Chemical Physics **147**, 164201 (2017).
[14] K. O. Tan, C. Yang, R. T. Weber, G. Mathies, and R. G. Griffin, Time-optimized pulsed dynamic nuclear polarization, Science Advances **5**, eaav6909 (2019).
[15] V. S. Redrouthu and G. Mathies, Efficient pulsed dynamic nuclear polarization with the x-inverse-x sequence, Journal of the American Chemical Society **144**, 1513 (2022).
[16] V. S. Redrouthu, S. Vinod-Kumar, and G. Mathies, Dynamic nuclear polarization by two-pulse phase modulation, The Journal of Chemical Physics **159**, 014201 (2023).
[17] N. Wili, A. B. Nielsen, L. A. Völker, L. Schreder, N. C. Nielsen, G. Jeschke, and K. O. Tan, Designing broadband pulsed dynamic nuclear polarization sequences in static solids, Science Advances **8**, eabq0536 (2022).
[18] M. Mardini, R. S. Palani, I. M. Ahmad, S. Mandal, S. K. Jawla, E. Bryerton, R. J. Temkin, S. T. Sigurdsson, and R. G. Griffin, Frequency-swept dynamic nuclear polarization, Journal of Magnetic Resonance **353**, 107511 (2023).
[19] A. B. Nielsen and N. C. Nielsen, Accurate analysis and perspectives for systematic design of magnetic resonance experiments using single-spin vector and exact effective hamiltonian theory, Journal of Magnetic Resonance Open **12-13**, 100064 (2022).
[20] R. Shankar, M. Ernst, P. K. Madhu, T. Vosegaard, N. C. Nielsen, and A. B. Nielsen, A general theoretical description of the influence of isotropic chemical shift in dipolar recoupling experiments for solid-state nmr, The Journal of Chemical Physics **146**, 134105 (2017).
[21] A. B. Nielsen, M. R. Hansen, J. E. Andersen, and T. Vosegaard, Single-spin vector analysis of strongly coupled nuclei in tocsy nmr experiments, The Journal of Chemical Physics **151**, 134117 (2019).

[22] U. Haeberlen and J. S. Waugh, Coherent averaging effects in magnetic resonance, Phys. Rev. **175**, 453 (1968).

[23] M. Hohwy and N. C. Nielsen, Systematic design and evaluation of multiple-pulse experiments in nuclear magnetic resonance spectroscopy using a semi-continuous baker–campbell–hausdorff expansion, The Journal of Chemical Physics **109**, 3780 (1998).

[24] O. Weintraub and S. Vega, Floquet density matrices and effective hamiltonians in magic-angle-spinning nmr spectroscopy, Journal of Magnetic Resonance, Series A **105**, 245 (1993).

[25] I. Scholz, J. D. van Beek, and M. Ernst, Operator-based floquet theory in solid-state nmr, Solid State Nuclear Magnetic Resonance **37**, 39 (2010).

[26] T. S. Untidt and N. C. Nielsen, Closed solution to the baker-campbell-hausdorff problem: Exact effective hamiltonian theory for analysis of nuclear-magnetic-resonance experiments, Phys. Rev. E **65**, 021108 (2002).

[27] D. Siminovitch, T. Untidt, and N. C. Nielsen, Exact effective hamiltonian theory. ii. polynomial expansion of matrix functions and entangled unitary exponential operators, The Journal of Chemical Physics **120**, 51 (2004), https://doi.org/10.1063/1.1628216.

[28] C. Jeffries, Polarization of nuclei by resonance saturation in paramagnetic crystals, Physical Review **106**, 164 (1957).

[29] C. Jeffries, Dynamic orientation of nuclei by forbidden transitions in paramagnetic resonance, Physical Review **117**, 1056 (1960).

[30] B. Blümich and H. Spiess, Quaternions as a practical tool for the evaluation of composite rotations, Journal of Magnetic Resonance (1969) **61**, 356 (1985).

[31] A. Wokaun and R. R. Ernst, Selective excitation and detection in multilevel spin systems: Application of single transition operators, The Journal of Chemical Physics **67**, 1752 (1977).

[32] S. Vega, Fictitious spin 1/2 operator formalism for multiple quantum NMR, The Journal of Chemical Physics **68**, 5518 (1978).

[33] N. Khaneja, T. Reiss, C. Kehlet, T. Schulte-Herbrüggen, and S. J. Glaser, Optimal control of coupled spin dynamics: design of nmr pulse sequences by gradient ascent algorithms, Journal of Magnetic Resonance **172**, 296 (2005).

[34] C. T. Kehlet, A. C. Sivertsen, M. Bjerring, T. O. Reiss, N. Khaneja, S. J. Glaser, and N. C. Nielsen, Improving solid-state nmr dipolar recoupling by optimal control, Journal of the American Chemical Society **126**, 10202 (2004).

[35] Z. Tošner, S. J. Glaser, N. Khaneja, and N. C. Nielsen, Effective hamiltonians by optimal control: Solid-state nmr double-quantum planar and isotropic dipolar recoupling, The Journal of Chemical Physics **125**, 184502 (2006).

[36] I. I. Maximov, Z. Tošner, and N. C. Nielsen, Optimal control design of nmr and dynamic nuclear polarization experiments using monotonically convergent algorithms, The Journal of Chemical Physics **128**, 184505 (2008).

[37] Z. Tošner, T. Vosegaard, C. Kehlet, N. Khaneja, S. J. Glaser, and N. C. Nielsen, Optimal control in nmr spectroscopy: Numerical implementation in simpson, Journal of Magnetic Resonance **197**, 120 (2009).

[38] D. L. Goodwin and I. Kuprov, Modified newton-raphson grape methods for optimal control of spin systems, The Journal of Chemical Physics **144**, 204107 (2016).

[39] M. S. Vinding, I. I. Maximov, Z. Tošner, and N. C. Nielsen, Fast numerical design of spatial-selective rf pulses in mri using krotov and quasi-newton based optimal control methods, The Journal of Chemical Physics **137**, 054203 (2012).

[40] H. Yuan, R. Zeier, N. Pomplun, S. J. Glaser, and N. Khaneja, Time-optimal polarization transfer from an electron spin to a nuclear spin, Phys. Rev. A **92**, 053414 (2015).

[41] P. Kaelo and M. M. Ali, Some variants of the controlled random search algorithm for global optimization, Journal of Optimization Theory and Applications **130**, 253 (2006).

[42] W. Price, A controlled random search procedure for global optimization, in 'towards global optimization 2', edited by lcw dixon and gp szegö (1978).

[43] W. Price, Global optimization by controlled random search, Journal of optimization theory and applications **40**, 333 (1983).

[44] T. H. Rowan, *Functional stability analysis of numerical algorithms*, Ph.D. thesis, Department of Computer Science, University of Texas at Austin, Austin, TX (1990).

[45] J. A. Nelder and R. Mead, A Simplex Method for Function Minimization, The Computer Journal **7**, 308 (1965).

[46] G. Guennebaud, B. Jacob, *et al.*, Eigen v3, http://eigen.tuxfamily.org (2010).

[47] S. G. Johnson, The NLopt nonlinear-optimization package, `https://github.com/stevengj/nlopt` (2007).

[48] R. Gupta, G. Hou, T. Polenova, and A. J. Vega, Rf inhomogeneity and how it controls CPMAS, Solid state nuclear magnetic resonance **72**, 17 (2015).